





Space group determination and first-principles structure optimization of the A-site ordered perovskite-type manganite $\text{NdBaMn}_2\text{O}_6$

Md Shafiqul Islam ^{1,*}, Daisuke Morikawa ¹, Shigeki Yamada,² Bikas Aryal ^{1,3}, Kenji Tsuda ³ and Masami Terauchi¹

¹*Institute of Multidisciplinary Research for Advanced Materials, Tohoku University, 2-1-1 Katahira, Aoba-ku, Sendai 980-8577, Japan*

²*Department of Materials System Science, Yokohama City University, Yokohama 236-0027, Japan*

³*Frontier Research Institute for Interdisciplinary Sciences, Tohoku University, Aramaki aza Aoba 6-3, Aoba-ku, Sendai 980-8578, Japan*



(Received 17 November 2021; revised 9 April 2022; accepted 20 May 2022; published 31 May 2022)

Space groups and crystal structures of A-site ordered $\text{NdBaMn}_2\text{O}_6$ perovskite have been investigated by a combination of selected-area electron diffraction (SAED), convergent-beam electron diffraction (CBED), and first-principles methods at high-temperature (HT ≈ 450 K), room-temperature (RT ≈ 293 K), and low-temperature (LT ≈ 95 K) phases. By symmetry analysis of the CBED patterns, space groups of $\text{NdBaMn}_2\text{O}_6$ at HT, RT, and LT phases have been determined to be $P4/mmm$ (No. 123), $C2mm$ (No. 38), and $P2_1am$ (No. 26), respectively. The space groups and the optimized structures using first-principle calculations at the HT and RT phases allow a single crystallographic site for Mn atoms, indicating no charge ordering state. At the LT phase, the observed SAED and CBED patterns revealed the existence of fourfold periodicity along the c axis compared with the pseudocubic unit cell. The optimized structure of the LT phase suggested four inequivalent Mn sites classified into two crystallographically different MnO_2 layers. Moreover, the structure showed that the four distinct MnO_6 octahedra are similarly compressed in the apical direction.

DOI: [10.1103/PhysRevB.105.174114](https://doi.org/10.1103/PhysRevB.105.174114)

I. INTRODUCTION

A-site ordered perovskite-type manganites with the chemical formula $R\text{BaMn}_2\text{O}_6$, where $R = \text{Y}$ and rare-earth elements, have been widely studied in recent years because of their rich and intriguing electronic and magnetic properties [1–6]. The origin of their large variety of exciting properties is the strong correlation among spin, charge, orbital, and lattice degrees of freedom [7–10]. Such correlation is significantly influenced by the trivalent R elements. Recently, several researchers have successfully synthesized $R\text{BaMn}_2\text{O}_6$ [9,11–13] in which RO , MnO_2 , and BaO layers are stacked alternately along the c axis. This stacking creates a MnO_2 square sublattice sandwiched by RO and BaO rock-salt layers with different lattice sizes. According to the crystal structure and mismatch between different layers, $R\text{BaMn}_2\text{O}_6$ can be classified into three groups [13,14]. The first group ($R = \text{Y, Tb, Dy, Ho}$) has the largest mismatch, resulting in large octahedral tilting, and exhibits three successive phase transitions, namely, structural transition, charge-ordered and orbital-ordered (CO-OO) transition associated with a metal-insulator (MI) transition, and antiferromagnetic metal (AFM) transition. On the other hand, the materials with $R = \text{Sm, Eu, Gd}$ having marginal tilt in the MnO_2 octahedra exhibit CO-OO transition followed by AFM transition [14]. These CO-OO states are stabilized above room temperature (RT) [7,8,15–18]. Because of the large ion size, the third group ($R = \text{La, Pr, Nd}$) prevents octahedral tilting at RT [13,14] and a ferromagnetic metal (FM) transition is followed

by an A-type AFM transition during cooling. Unlike other A-site ordered manganites, $\text{NdBaMn}_2\text{O}_6$ is unique because it is located in close vicinity of the multicritical point where the CO-OO, A-type AFM, and FM phases compete with each other [8,19]. X-ray diffraction (XRD) study using polycrystalline samples [20] revealed that the crystal structure of $\text{NdBaMn}_2\text{O}_6$ at 400 K has a tetragonal $a_{\text{pc}} \times b_{\text{pc}} \times 2c_{\text{pc}}$ unit cell with a space group of $P4/mmm$, where a_{pc} , b_{pc} , and c_{pc} are the lattice parameters of the pseudocubic perovskite structure. In neutron diffraction measurements using powder samples, $\text{NdBaMn}_2\text{O}_6$ exhibits a paramagnetic metal (PM) to FM transition at 300 K, followed by FM to A-type AFM transition at 290 K which coincides with $d_{x^2-y^2}$ orbital ordering in the ab plane [8,20]. The single-crystal XRD studies at a high-temperature (HT) phase above 370 K determined the space group as $P4/mmm$ with tetragonal structure of lattice parameters $a = 3.911$ Å and $c = 7.7577$ Å [21,22]. They concluded that the space group at the RT phase extended from 370 to 290 K is $Cmmm$ (No. 65) with orthorhombic cell of dimensions $2a_{\text{pc}} \times 2b_{\text{pc}} \times 2c_{\text{pc}}$. The onset of an MI transition at 290 K is caused by a structural phase transition coupled with $d_{x^2-y^2}$ orbital ordering, which agrees with the finding of previous studies on polycrystalline samples [8,20]. In the low-temperature (LT) phase below 290 K, the space group is determined to be $P2_1am$ with orthorhombic unit cell of $\sqrt{2}a_{\text{pc}} \times \sqrt{2}b_{\text{pc}} \times 2c_{\text{pc}}$. Raman spectroscopy measurements show that the phonon mode associated with Jahn-Teller octahedra distortion is enhanced dramatically at LT, which indicates the orbital ordering in $\text{NdBaMn}_2\text{O}_6$ [23]. However, a recent study suggests that there is no orbital ordering in the orthorhombic ab plane at the LT phase [22]. So far, the structural properties of $\text{NdBaMn}_2\text{O}_6$ have been studied by

*islam.md.shafiqul.q2@dc.tohoku.ac.jp

means of XRD and neutron diffraction techniques. Especially at the LT phase, the crystal structure has not been deeply studied because of imperfection of the crystal structure, multiple scattering, and the self-absorption problem for XRD and neutron diffraction methods [14,22]. Therefore, a new approach is essential for precise structure analysis.

Convergent-beam electron diffraction (CBED) is one of the most powerful diffraction techniques to determine the crystal symmetry through a strong dynamical diffraction effect [24–29]. Depending on the symmetry appearing in the CBED patterns, the crystal point group and the space group can uniquely be determined. In particular, the CBED method can distinguish polar structures from nonpolar structures on the basis of the dynamical diffraction effect. Moreover, the symmetry of the CBED pattern is very sensitive to crystal defects, which enable us to obtain the CBED pattern from the specimen area without any defects or *ab* twin structure [30–32].

In the present study, the space group and crystal structure of $\text{NdBaMn}_2\text{O}_6$ have been investigated at high-temperature (HT ≈ 450 K), room-temperature (RT ≈ 293 K), and low-temperature (LT ≈ 95 K) phases. For determining the space group, the CBED method is used, whereas to understand the structure at each temperature phase, structure optimization is performed using first-principles methods. It is found that the optimized structures can well reproduce the experimental CBED patterns.

II. EXPERIMENTAL AND THEORETICAL METHODS

A. Electron diffraction measurements

Single crystals of $\text{NdBaMn}_2\text{O}_6$ were grown using the floating zone (FZ) technique [21]. For electron diffraction experiments, specimens were prepared by crushing the bulk single crystals and gluing the small fragments onto copper grids. All the experiments were conducted by using an energy filter transmission electron microscope, JEM-2010FEF, equipped with a field-emission gun and an Omega (Ω)-type energy filter, operated at an accelerating voltage of 100 kV. The size of the electron probe used to obtain CBED patterns was about 1 nm in diameter. Selected-area electron diffraction (SAED) and CBED patterns were recorded on imaging plates (IPs) in order to observe very weak intensities and read out using the imaging-plate reader DITABIS micron with a 20-bit dynamic range. High-temperature observations were performed at 450 K by using a double-tilt heating holder. A double-tilt liquid nitrogen cooling holder was used for LT measurement at 95 K.

B. Structure optimization

For structure optimization, the first-principles calculations based on density functional theory (DFT) [33,34], plane waves, and pseudopotentials [35] approaches are carried out by the QUANTUM ESPRESSO simulation package [36,37]. In an effort to obtain the lowest-energy structure at each temperature phase, the initial structure has been relaxed until the total energy and the total force per atom is less than 10^{-8} Ry and 10^{-4} Ry/a.u., respectively. Brillouin zone sampling is performed by the Monkhorst-Pack scheme [38] with $4 \times 4 \times 2$

k -point mesh for the HT phase, $4 \times 4 \times 4$ k -point mesh for the HT phase, and $4 \times 6 \times 2$ k -point mesh for the LT phase, respectively. The plane-wave cutoff energy is set to be 60 Ry in all the calculations. In order to treat electron-ion interaction, an ultrasoft pseudopotential (USPP) [39] with nonlinear core correction is used. The Perdew-Burke-Ernzerhof (PBE) functionals within generalized gradient approximation (GGA) are adopted as the exchange-correlation functional [40].

In a particular temperature phase, a model structure is created by estimating the atomic positions allowed by the determined space group. From this structure, several model structures are generated by changing the positions of atoms in particular O and Mn atoms. For example, at RT, around 10 distinct model structures are generated by different combination of O and Mn positions in the unit cell. The new arrangement of O and Mn atomic positions introduces an octahedral distortion and/or an octahedral rotation in the structure. After that, the model structures are relaxed by performing structure optimization. Using the relaxed structures, the experimental CBED patterns are simulated based on dynamical electron diffraction theory. Finally, one of the relaxed structures is selected as the optimized structure by qualitative comparison between experimental and simulated CBED patterns at high-symmetry incidences, such as [001], [010], and [100].

C. Dynamical diffraction calculation

The crystal structures obtained from first-principles DFT calculation are used to reproduce the experimentally obtained CBED patterns. Theoretical intensities of the CBED patterns at each temperature phase are simulated on the basis of many-beam dynamical electron diffraction theory as implemented in the MBFIT simulation package [41–43]. Generally, the intensities of higher-order Laue zone (HOLZ) reflections, having large reciprocal lattice vectors \mathbf{g} , are more sensitive to the displacements of atoms than those of zeroth-order Laue zone (ZOLZ) reflections. For this reason, the HOLZ reflections can effectively be used for the accurate determination of the atomic positions [41,42]. However, only the HOLZ reflections at one incidence are not sufficient to obtain three-dimensional (3D) information of the structure. In order to recover the 3D structural information, the CBED patterns were taken at [001], [100], and [010] incidences.

III. RESULTS AND DISCUSSION

A. Space group at HT

Figures 1(a) and 1(b) show the SAED patterns of $\text{NdBaMn}_2\text{O}_6$ at HT (≈ 450 K) taken from [001] and [100] incidences, respectively. The reflection spots are indexed on the basis of a tetragonal unit cell with lattice parameters, $a_{\text{HT}} = 3.9110$ Å, $b_{\text{HT}} = 3.9110$ Å, and $c_{\text{HT}} = 7.7577$ Å [21]. The dimensions of the unit cell are $a_{\text{pc}} \times b_{\text{pc}} \times 2c_{\text{pc}}$. Doubling of the unit cell along the c axis is due to the A -site ordering of Nd and Ba atoms. As there are no extinction rules due to the lattice that are observed, the type of lattice is determined to be primitive.

The CBED patterns of $\text{NdBaMn}_2\text{O}_6$ taken at HT are shown in Fig. 2. Conventionally, the ZOLZ reflections are observed in the center of the pattern, which is enlarged with

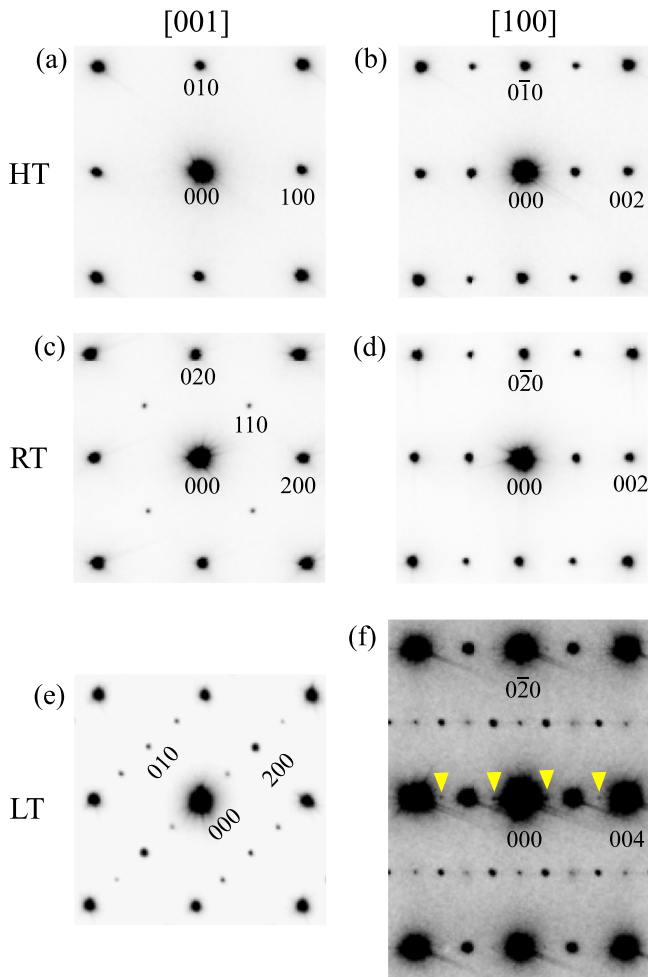


FIG. 1. SAED patterns of $\text{NdBaMn}_2\text{O}_6$ at three different temperature phases. SAED patterns taken at HT with (a) [001] and (b) [100] zone axis incidences. For the same incidences, the patterns are obtained at (c),(d) RT and (e),(f) LT, respectively. For the HT phase, the diffraction spots in (a) and (b) are indexed on the basis of tetragonal symmetry. The diffraction spots in (c) and (d) are indexed as orthorhombic unit cell. The forbidden condition $hk0 = 2n + 1$, where n is an integer, coincides with a C -centered lattice. At the LT phase, all diffraction spots in (e) and (f) are indexed considering orthorhombic symmetry. The yellow arrowheads in (f) indicate the weak reflection spots $00l$, where l is an odd integer.

increasing contrast in Figs. 2(a) and 2(b). In addition to the ZOLZ reflection, first-order Laue zone (FOLZ) reflections and second-order Laue zone (SOLZ) reflections are termed as HOLZ, appearing as ring-shaped diffraction disks surrounding the ZOLZ reflections, as shown in Fig. 2(a). It is worth mentioning that the FOLZ reflections in Fig. 2(a) are superlattice reflections along the incident beam direction, showing the duplication of the unit cell in the c -axis direction due to the presence of the distortion of the perovskite structure from its ideal cubic structure and the stacking manner of octahedron along the incident beam direction [29].

The FOLZ reflections at [001] incidence, as indicated in Fig. 2(a), having weak intensities, mainly appear due to A -site ordering. In order to confirm symmetry, SOLZ reflections are

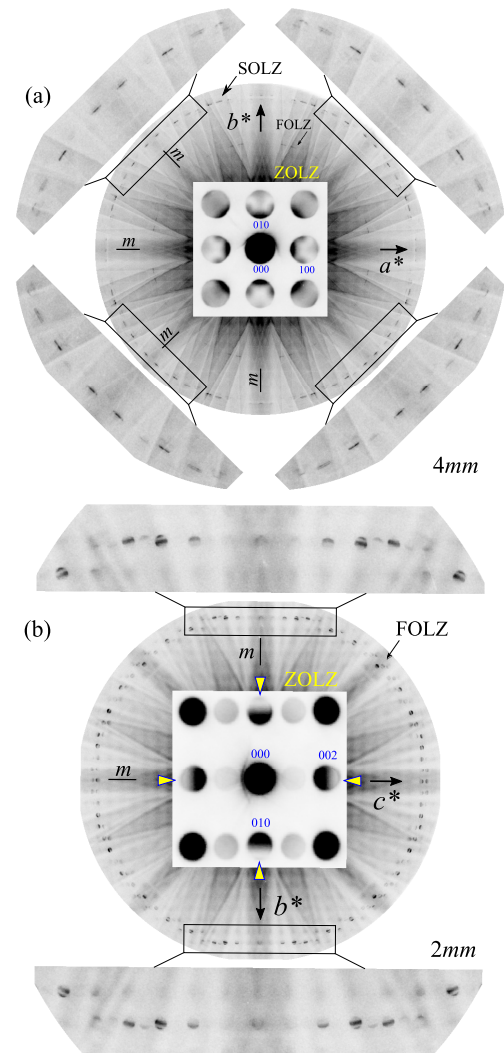


FIG. 2. CBED patterns of $\text{NdBaMn}_2\text{O}_6$ at HT taken with (a) [001] and (b) [100] incidences. Here, m indicates the mirror symmetry parallel to electron incidence. Enlarged SOLZ pattern in (a) and enlarged FOLZ pattern in (b) explicitly show $4mm$ and $2mm$ symmetries, respectively. The yellow arrowheads in the ZOLZ pattern in (b) indicate that the reflections have mirror symmetry.

used. The enlarged SOLZ reflections exhibit $4mm$ symmetry, i.e., fourfold rotational symmetries and two types of mirror symmetries. The ZOLZ reflections enlarged in the center of Fig. 2(a) show a symmetry of $4mm$. Therefore, the whole CBED pattern of Fig. 2(a) is concluded to have $4mm$ symmetry. As depicted in Fig. 2(b), the whole CBED pattern at [100] incidence shows $2mm$ symmetry. These results indicate that the point group of $\text{NdBaMn}_2\text{O}_6$ at HT is $4/mmm$. Thus, the possible space group candidates are from No. 123 to No. 138 for point group $4/mmm$ with primitive lattice. In order to confirm the space group, it is essential to check the presence of the dynamical extinction lines (DELs) in the CBED reflection disks [26,28,29]. The presence of the DELs indicates that a screw axis and/or glide plane exist parallel or perpendicular to the electron beam incidence. However, there are no DELs observed in the CBED disks at [001] and [100] incidences.

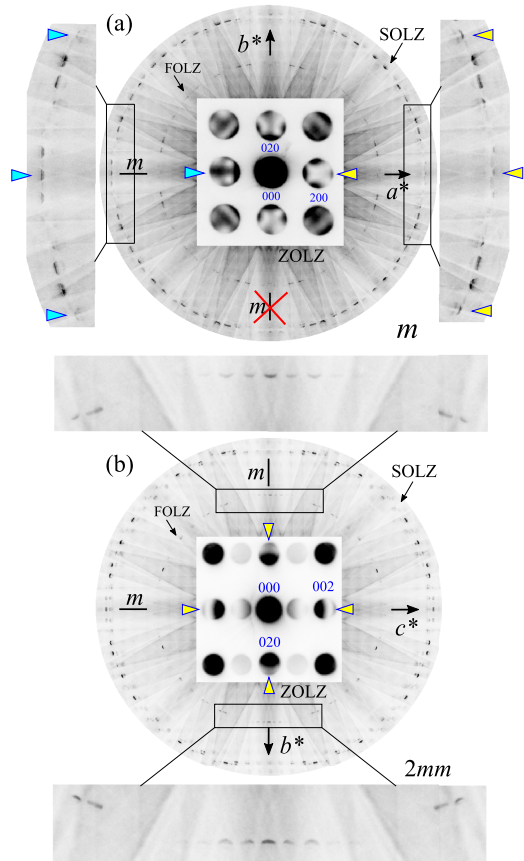


FIG. 3. CBED patterns of $\text{NdBaMn}_2\text{O}_6$ at RT taken with (a) [001] and (b) [100] incidences. Here, m indicates the mirror symmetry parallel to the electron incidence. The ZOLZ pattern in (a) clearly exhibits the breakdown of mirror symmetry perpendicular to the a axis. The yellow and blue arrowheads in the ZOLZ and SOLZ patterns indicate that the reflections have no mirror symmetry. The ZOLZ and enlarged FOLZ patterns in (b) shows $2mm$ symmetry. The yellow arrowheads in the ZOLZ pattern indicate that the reflections have mirror symmetry.

Therefore, the space group of $\text{NdBaMn}_2\text{O}_6$ at HT has been uniquely determined to be $P4/mmm$ (No. 123).

B. Space group at RT

The SAED patterns of $\text{NdBaMn}_2\text{O}_6$ at RT (≈ 293 K) taken at [001] and [100] incidences are shown in Figs. 1(c) and 1(d), respectively. All the reflection spots are indexed assuming an orthorhombic unit cell of $2a_{pc} \times 2b_{pc} \times 2c_{pc}$ with lattice parameters, $a_{RT} = 7.8148$ Å, $b_{RT} = 7.7877$ Å, and $c_{RT} = 7.7281$ Å [21].

Figure 3 shows the CBED patterns of $\text{NdBaMn}_2\text{O}_6$ taken at [001] and [100] incidences. Both of the ZOLZ and the SOLZ reflections at [001] incidence exhibit a mirror symmetry perpendicular to the b axis, but a break down of the mirror symmetry perpendicular to the a axis, as shown in Fig. 3. The whole CBED pattern at [010] incidence clearly shows no mirror symmetry perpendicular to the a axis, as shown in Fig. S1 in the Supplemental Material [44]. From these observations, it is evident that there is no mirror symmetry perpendicular to the a axis. As shown in Fig. 3(b),

the ZOLZ reflection disks clearly show $2mm$ symmetry. The enlarged FOLZ pattern exhibits $2mm$ symmetry. To ensure $2mm$ symmetry at [100] incidence, the CBED patterns with a slight tilting along the b axis and c axis are taken, as shown in Fig. S2 in the Supplemental Material [44]. Therefore, at RT, the point group of $\text{NdBaMn}_2\text{O}_6$ is confirmed to be $2mm$.

The disappearance of $hk0$ ($h+k=2n+1$, where n is an integer) reflections ensures that the lattice of $\text{NdBaMn}_2\text{O}_6$ is the C -centered type. As a result, the possible space groups are from No. 38 to No. 41. Since the DELs in the $00l$ (l ; odd) reflection disks at [100] incidence are not found, as shown in Fig. 3(b), the possibilities of No. 40 and No. 41 can be eliminated. The remaining two possible candidates are $C2mm$ (No. 38) and $C2mb$ (No. 39). Between them, $C2mb$ can be omitted because there are no DELs observed in the $h\bar{k}0$ (h, \bar{k} ; odd) reflection disks at [110] incidence, as shown in Fig. S3 in the Supplemental Material [44]. Therefore, the space group of $\text{NdBaMn}_2\text{O}_6$ at RT has been unambiguously determined as $C2mm$ (No. 38).

However, the present $C2mm$ (No. 38) space group is incompatible with $Cmmm$ (No. 65) reported by previous XRD studies [21,22]. Although, in the single-crystal XRD structure analysis [21], both $C2mm$ ($R = 4.02\%$ and $R_w = 7.87\%$) and $Cmmm$ ($R = 3.06\%$ and $R_w = 5.98\%$) phases were obtained, $Cmmm$ (No. 65) was instead selected due to the R factors and smooth convergence of the structure refinement parameters. It is noted that the XRD study was performed using a single crystal of $\text{NdBaMn}_2\text{O}_6$ including ab twin structures [21], which can be a reason for this inconsistency. On the other hand, the powder XRD measurement [22] is not influenced by such twin structures of the sample. In this case, the insensitivity of the XRD to distinguish a polar structure from a nonpolar structure, which is due to Friedel's law of the kinematical diffraction theory, could be a reason for the conclusion of $Cmmm$ (No. 65) instead of $C2mm$ (No. 38).

C. Space group at LT

For the LT (≈ 95 K) phase, the SAED patterns taken at [001] and [100] incident directions are shown in Figs. 1(e) and 1(f), respectively. It should be noted that the a and b axes in the LT phase are rotated by 45 degrees with respect to the RT and HT phases, as shown in Figs. 1(a), 1(c) and 1(e). The reflection spots of the SAED patterns, as shown in Figs. 1(e) and 1(f), are indexed by considering the orthorhombic unit cell of $2\sqrt{2}a_{pc} \times \sqrt{2}b_{pc} \times 4c_{pc}$ with lattice parameters $a_{LT} = 11.1100$ Å, $b_{LT} = 5.5550$ Å, and $c_{LT} = 15.2420$ Å estimated from the pseudocubic unit cell. In Fig. 1(e), the presence of weak reflection spots $00l$ (l ; odd) at [100] incidence, as indicated by yellow arrowheads, discloses that the unit cell of $\text{NdBaMn}_2\text{O}_6$ at LT is four times longer along the c axis than that of the pseudocubic perovskite structure. On the other hand, former XRD studies reported that the unit cell has twofold periodicity along the c axis with cell dimensions $\sqrt{2}a_{pc} \times \sqrt{2}b_{pc} \times 2c_{pc}$ [21,22]. This discrepancy may arise due to the low sensitivity of the XRD technique to detect weak reflection spots.

Figure 4 shows the CBED patterns of $\text{NdBaMn}_2\text{O}_6$ at LT. At [001] incidence, the CBED patterns as a whole exhibit a mirror symmetry perpendicular to the b axis, but no mirror

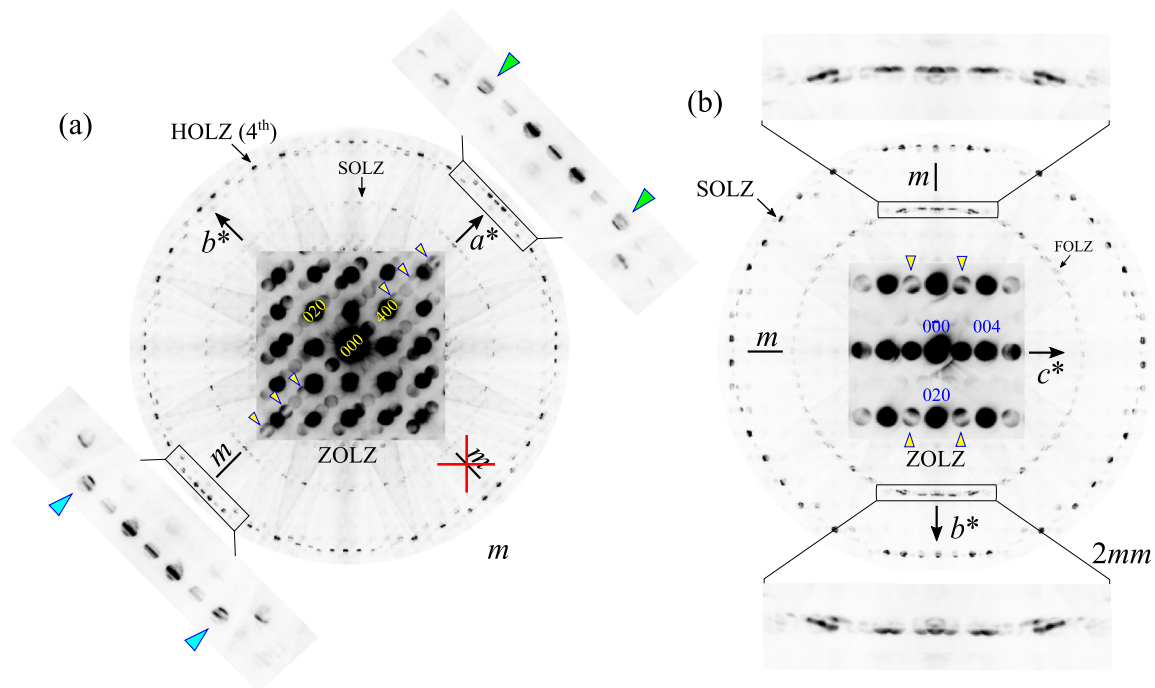


FIG. 4. CBED patterns of $\text{NdBaMn}_2\text{O}_6$ at LT taken with (a) $[001]$ and (b) $[100]$ incidences. Here, m indicates the mirror symmetry parallel to the electron incidence. The enlarged fourth-order HOLZ pattern in (a) ensures that there is no mirror symmetry perpendicular to the a axis. The blue and green arrowheads indicate that the reflections have no mirror symmetry. The yellow arrowheads in the ZOLZ pattern point out $h00$ (h ; odd) reflection disks in which dynamical extinction lines have appeared. The ZOLZ and enlarged FOLZ patterns in (b) shows $2mm$ symmetry. The yellow arrowheads in the ZOLZ pattern indicate that the reflection disks have mirror symmetry.

symmetry perpendicular to the a axis, as shown in Fig. 4(a) by enlarging the HOLZ pattern. The whole CBED pattern at $[100]$ incidence shows $2mm$ symmetry, which is clearly seen in the enlarged portion of FOLZ reflections in Fig. 4(b). The tilted CBED patterns for both $[001]$ and $[100]$ incidences are presented in Fig. S4 in the Supplemental Material [44]. These results indicate that the point group of $\text{NdBaMn}_2\text{O}_6$ at LT is $2mm$.

The lattice is determined to be primitive as extinction rules due to the lattice type are not observed. Thus, the possible space groups for the point group $2mm$ and primitive cell are from No. 25 to No. 34. As shown in Fig. 4(a), A_2 -type DELs are observed in the $h00$ (h ; odd) reflection disks at $[001]$ incidence, as indicated by yellow arrowheads. These conditions are only consistent with the space group candidate $P2_1am$ (No. 26). Therefore, the space group at the LT phase has been uniquely determined as $P2_1am$ (No. 26).

D. Structure analysis

The optimized crystal structure of $\text{NdBaMn}_2\text{O}_6$ at each temperature phase is selected by qualitative comparison between experimental and simulated intensities of the HOLZ reflections at $[001]$, $[010]$, and $[100]$ incidences. The optimized structure parameters at the HT, RT, and LT phases are listed in Table I and the three-dimensional (3D) view of the crystal structures is shown in Fig. S5 in the Supplemental Material [44].

Figures 5(a) and 5(b) show the experimental and the simulated intensities of the HOLZ reflections with respect to

$[100]$ incidence at RT. The positions and the intensity distribution of the simulated SOLZ reflections almost reproduce the experimental SOLZ reflections, as displayed by enlarging the rectangular portion in Fig. 5 and in Fig. S6 in the Supplemental Material [44]. At $[001]$ incidence, the simulated HOLZ reflections can well reproduce the breakdown of mirror symmetry perpendicular to the a axis and the intensities distribution of the experimental HOLZ reflections, which is shown in Fig. S7 in the Supplemental Material [44]. In the case of HT and LT phases, the positions and the intensity distribution of the simulated HOLZ reflections are comparable with that

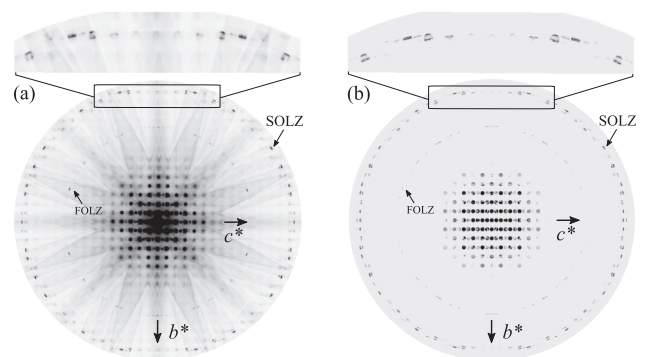


FIG. 5. (a) Experimental and (b) simulated CBED patterns of $\text{NdBaMn}_2\text{O}_6$ at RT with respect to $[100]$ incidence. The enlarged CBED pattern displays the similarity between experimental and simulated positions and intensity distribution of the SOLZ reflection disks.

TABLE I. Optimized structures of NdBaMn₂O₆ at HT, RT, and LT. For structure optimization at the HT and LT phases, the lattice parameters reported by XRD measurement [21] have been used. In the case of the LT phase, the lattice parameters are estimated from the pseudocubic unit cell. The valence state of Mn ions is estimated by the bond valence sum (BVS) detailed in Table S3 in the Supplemental Material [44]. The calculated BVS of the Mn ion at the HT phase is $V_{\text{BVS}} = 3.489$. For the RT phase, the BVS of the Mn ion is $V_{\text{BVS}} = 3.429$. At the LT phase, the BVS of the Mn1, Mn2, Mn3, and Mn4 ions is 3.517, 3.511, 3.518, and 3.512, respectively.

	Atom	Site	x	y	z
$T = 450 \text{ K } (P4/mmm)$ $a = 3.9110 \text{ \AA}$ $c = 7.7577 \text{ \AA}$ $V = 118.6612 \text{ \AA}^3$	Nd	1a	0	0	0
	Ba	1b	0	0	0.5
	Mn	2h	0.5	0.5	0.2462
	O1	1c	0.5	0.5	0
	O2	1d	0.5	0.5	0.5
	O3	4i	0	0.5	0.2263
$T = 293 \text{ K } (C2mm)$ $a = 7.8148 \text{ \AA}$ $b = 7.7877 \text{ \AA}$ $c = 7.7281 \text{ \AA}$ $V = 470.3268 \text{ \AA}^3$	Nd1	2a	0.2428	0	0
	Nd2	2a	0.7448	0	0
	Ba1	2b	0.7549	0	0.5
	Ba2	2b	0.2545	0	0.5
	Mn	8f	0.0037	0.25003	0.2493
	O1	4d	0.0123	0.7533	0
	O2	4e	0.0049	0.2508	0.5
	O3	4c	0.5072	0	0.2249
	O4	4c	0.0061	0	0.2288
	O5	8f	0.2568	0.2495	0.2258
$T = 95 \text{ K } (P2_1am)$ $a = 11.1100 \text{ \AA}$ $b = 5.5550 \text{ \AA}$ $c = 15.2420 \text{ \AA}$ $V = 940.6759 \text{ \AA}^3$	Nd1	2a	0.0090	0.5003	0
	Nd2	2b	0.0095	0.5083	0.5
	Nd3	2a	0.2433	0.9952	0
	Nd4	2b	0.2439	0.0013	0.5
	Ba1	4c	0.0044	0.5022	0.2499
	Ba2	4c	0.2487	0.9989	0.2499
	Mn1	4c	0.9985	0.0010	0.1249
	Mn2	4c	0.9986	0.0042	0.6249
	Mn3	4c	0.2544	0.4973	0.1249
	Mn4	4c	0.2544	0.4997	0.6249
	O1	2a	0.0150	0.9989	0
	O2	2b	0.0146	0.00003	0.5
	O3	4c	0.9955	0.0022	0.2499
	O4	2a	0.2387	0.4989	0
O5	2b	0.2379	0.4989	0.5	
O6	4c	0.2575	0.4988	0.2499	
O7	4c	0.1263	0.2496	0.1174	
O8	4c	0.1265	0.2510	0.6178	
O9	4c	0.3766	0.2485	0.1091	
O10	4c	0.3764	0.2482	0.6082	
O11	4c	0.1270	0.7496	0.1172	
O12	4c	0.1262	0.7509	0.6171	
O13	4c	0.3767	0.7485	0.1079	
O14	4c	0.3763	0.7482	0.6087	

of experimental HOLZ reflections, as shown in Fig. S8 and Fig. S9 in the Supplemental Material [44]. The consistency of the positions and the intensity distribution between the experimental and the simulated HOLZ reflections indicate that the optimized structures are close enough to their corresponding real structures.

At HT and RT phases, the crystal structures have a single crystallographic site for Mn atoms as listed in Table I, indicating the absence of a charge ordering state, which is consistent with previously reported works [21,22]. For the optimized structure at the HT phase, four basal (over ab plane) Mn-O distances in MnO₆ octahedra are nearly equal to 1.962 Å,

while the average apical (along the c axis) Mn-O distance is about 1.939 Å, as shown in Fig. 6(a). The small difference in the apical Mn-O distance is mainly due to the shifting of O3 and Mn atoms toward the c axis. In the case of the RT structure, the average apical Mn-O distance is about 1.932 Å, where the average basal Mn-O distance is around 1.96 Å, as shown in Fig. 6(b). The small variation of the basal Mn-O distances comes from the shifting of O3, O4, O5, and Mn atoms toward the c axis. As the average apical and basal Mn-O distances at RT are almost comparable to that of HT, there is no significant compression or expansion of the octahedra, indicating no orbital ordering at HT and RT phases.

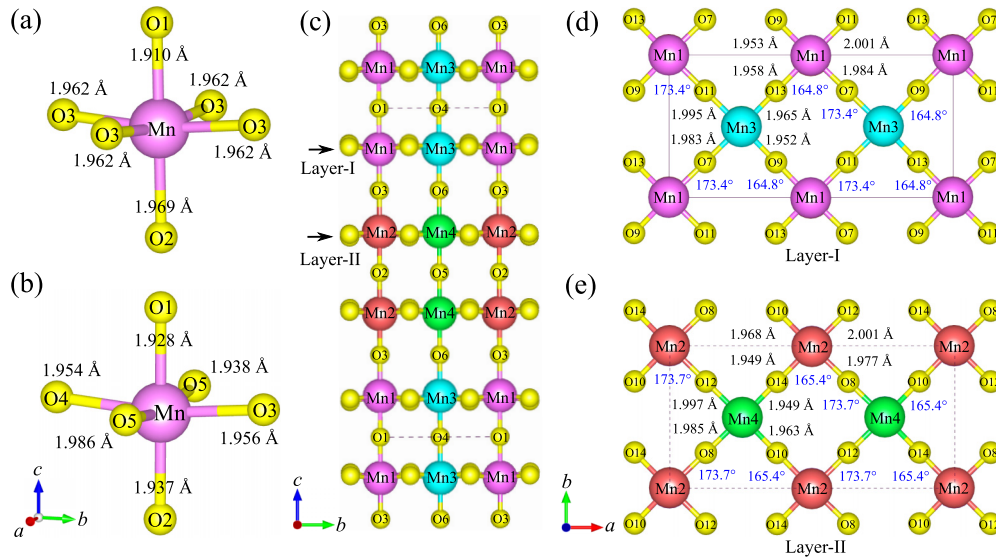


FIG. 6. Details of MnO_6 octahedra in the optimized structure of $\text{NdBaMn}_2\text{O}_6$ at (a) HT and (b) RT phases. Unit cell of $\text{NdBaMn}_2\text{O}_6$ at the LT phase with (c) a -axis view. The black arrows indicate the layers arranged along the c axis. The distribution of Mn-O distances in (d) layer I and (e) layer II. All MnO_6 octahedra have two long and two short Mn-O distances in the basal direction. The two long (short) Mn-O distances are orientated almost perpendicularly with each other. The average basal and apical Mn-O distances are about 1.974 Å and 1.91 Å, respectively. In (d), the $\langle \text{Mn1} - \text{O7} - \text{Mn3} \rangle$ and $\langle \text{Mn3} - \text{O13} - \text{Mn1} \rangle$ bond angles are about 173.4° and 164.8° , respectively. In (e), the $\langle \text{Mn2} - \text{O8} - \text{Mn4} \rangle$ and $\langle \text{Mn4} - \text{O14} - \text{Mn2} \rangle$ bond angles are about 173.7° and 165.4° , respectively.

At the LT phase, the crystal structure has fourfold periodicity along the c axis compared with a pseudocubic unit cell, and four nonequivalent Mn sites results in a larger and complicated structure. As shown in Fig. 6(c), two different types of MnO_2 layers, namely, layer I and layer II, are alternatively stacked by making a pair of similar layers along the c axis. For both of the layers, MnO_6 octahedra have a common characteristic where each octahedron has two long and two short basal Mn-O distances, as shown in Figs. 6(d) and 6(e). The average basal Mn-O distance is equivalent to 1.974 Å, whereas the average apical Mn-O distance is about 1.91 Å. It is clearly seen that the average apical Mn-O distance is smaller than the average basal Mn-O distance, which leads to compression of the MnO_6 octahedra. Moreover, the occupation of two short and two long Mn-O distances of each Mn site can lead to the unbalance of the net Mn-O distance along the a axis, which could be a reason for polarization in the a -axis direction.

However, on the basis of apically compressed MnO_6 octahedra, it is difficult to say whether it is owing to Jahn-Teller distortion or localization of the e_g electron. In order to explain MnO_6 octahedra distortion, two possible models can be proposed as follows.

First, consider that the apical compression of MnO_6 octahedra is due to Jahn-Teller coupling of $d_{x^2-y^2}$ orbital ordering reported in [21]. Then, such $d_{x^2-y^2}$ orbital ordering in $\text{NdBaMn}_2\text{O}_6$ is different from conventional $d_{3z^2-r^2}$ -type orbital ordering as occurred in $\text{La}_{0.5}\text{Sr}_{1.5}\text{MnO}_4$ and single-layer manganites [45]. For double-layered manganites, although the CO-OO unit-cell dimensions ($2\sqrt{2}a_{\text{pc}} \times \sqrt{2}b_{\text{pc}} \times 4c_{\text{pc}}$) of $\text{SmBaMn}_2\text{O}_6$ at RT [17] are the same as that of $\text{NdBaMn}_2\text{O}_6$ at LT, the previous works suggest $d_{3x^2-r^2}/d_{3y^2-r^2}$ orbital ordering in $\text{SmBaMn}_2\text{O}_6$ [17,46], whereas $\text{NdBaMn}_2\text{O}_6$ exhibits $d_{x^2-y^2}$ orbital ordering in the ab plane. As listed in Table I, the

calculated bond valence sums (BVSs) of crystallographically distinct Mn atoms at each layer, i.e., layer I ($\text{Mn1} = 3.517$, $\text{Mn3} = 3.518$) and layer II ($\text{Mn2} = 3.511$, $\text{Mn4} = 3.512$), show a negligible difference (≈ 0.001), which indicates no significant charge disproportionation between them. Thus, it is difficult to determine the occurrence of checkerboard-type charge ordering in the ab plane on the basis of the calculated BVS. If the charge ordering is realized between two crystallographically distinct Mn ions at each layer for $\text{NdBaMn}_2\text{O}_6$, it will be weak compared with $\text{SmBaMn}_2\text{O}_6$ due to small charge disproportionation. On the other hand, unlike within the same layer (≈ 0.001), the calculated BVSs show a little larger difference (≈ 0.006) between layer I and layer II, indicating a small difference of electrostatic potential distribution between layer I and layer II. Therefore, the periodic modulation of the different electrostatic potential distribution along the c axis could be a reason for the fourfold periodicity in the c direction.

For $\text{SmBaMn}_2\text{O}_6$ at RT, the significant amount of charge disproportionation between Mn ions ($\text{Mn}^{3+}/\text{Mn}^{4+}$) favors the crystallographically similar MnO_2 layers to stack along the c axis with a relative phase shift along the a axis [9,16,17,47]. In the case of $\text{NdBaMn}_2\text{O}_6$ at LT, the negligible charge disproportionation of Mn ions and similar distortion of all MnO_6 octahedra suggest the crystallographically distinct MnO_2 layers will stack without a relative phase shift.

Second, consider that MnO_6 octahedra distortion is due to localization of the e_g electron as reported in [22]. As shown in Figs. 6(d) and 6(e), two different $\langle \text{Mn} - \text{O} - \text{Mn} \rangle$ bond angles, around 165° and 173° , are alternatively arranged in the ab plane. The decrease of $\langle \text{Mn} - \text{O} - \text{Mn} \rangle$ bond angles and their alternating arrangement in the ab plane could be a reason for the localization of the e_g electron at the Mn sites. Moreover, the deviation of the $\langle \text{Mn} - \text{O} - \text{Mn} \rangle$ bond angle from 180° can stabilize a periodic arrangement of alternating

short and long Mn-O distances in the *ab* plane, as shown in Figs. 6(d) and 6(e).

However, only from space group and structure analysis, it would be tough to provide conclusive evidence for the presence of CO-OO states and polarization of the material. To resolve this problem, a first-principles electron density analysis could be a potential method.

IV. CONCLUSIONS

The space groups and the optimized structures of NdBaMn₂O₆ have been examined by a combination of CBED and first-principles methods at HT, RT, and LT phases, respectively. The space group of NdBaMn₂O₆ of the HT phase has been determined to be *P4/mmm* (No. 123) with cell dimensions of $a_{pc} \times b_{pc} \times 2c_{pc}$. At RT, the material undergoes a structural phase transition from a tetragonal to orthorhombic cell of dimensions $2a_{pc} \times 2b_{pc} \times 2c_{pc}$. The symmetry analysis of the observed CBED patterns at this temperature revealed that the space group is *C2mm* (No. 38). It was found that the optimized structures with determined space groups at HT and RT phases have one crystallographic site for Mn atoms, indicating the absence of a charge ordering state. In the case of the LT phase, the observation of the very weak intensity of $00l$ (l ; odd) reflection spots at $[100]$ incidence revealed that the unit cell is four times larger along the *c* axis compared with the pseudocubic cell. Based on the symmetry that appeared on the CBED patterns, the space group of the LT phase was determined to be *P2₁am* (No. 26) with an orthorhombic unit cell of $2\sqrt{2}a_{pc} \times \sqrt{2}b_{pc} \times 4c_{pc}$. The optimized structure at the LT phase has four inequivalent sites for Mn atoms and two types of MnO₂ layers stacking along the *c* axis. Moreover, the

optimized structure showed that four distinct MnO₂ octahedra are compressed in the *c*-axis direction. Such MnO₂ octahedra distortion can be attributed to either Jahn-Teller coupling of the orbital degree of freedom or localization of the e_g electron at the Mn sites. The imbalance of net Mn-O distances along the *a* axis can lead to the polarization of this material, which is allowed by the noncentrosymmetric space group *P2₁am* (No. 26).

However, although the space group and optimized structure suggested the alternative arrangement of two distinct Mn atoms at each layer, the BVS of the Mn ions showed insignificant charge disproportion between them. For this reason, only from such structure analysis, it is difficult to provide conclusive evidence about CO-OO states and polarization of the material at this moment. To better understand the structure at the LT phase, a first-principles electron density analysis can be an essential approach. Since the optimized structures can well reproduce the experimental CBED patterns, these are expected to be appropriate as initial structures for quantitative refinement of the structures. At present, the first-principles electron density analysis and quantitative crystal structure analysis are ongoing.

ACKNOWLEDGMENTS

The authors would like to thank Dr. Yohei Sato for the valuable discussions and Mr. Masaki Ageishi for his careful maintenance of the JEM-2010FEF transmission electron microscopes. M.S.I. acknowledges financial support through a MEXT scholarship. This work is partly supported by JSPS KAKENHI Grants No. JP20H05176 and No. JP18H03674.

-
- [1] R. von Helmolt, J. Wecker, B. Holzapfel, L. Schultz, and K. Samwer, *Phys. Rev. Lett.* **71**, 2331 (1993).
- [2] K.-I. Chahara, T. Ohno, M. Kasai, and Y. Kozono, *Appl. Phys. Lett.* **63**, 1990 (1993).
- [3] A. Urushibara, Y. Moritomo, T. Arima, A. Asamitsu, G. Kido, and Y. Tokura, *Phys. Rev. B* **51**, 14103 (1995).
- [4] H. Kuwahara, Y. Moritomo, Y. Tomioka, A. Asamitsu, M. Kasai, R. Kumai, and Y. Tokura, *Phys. Rev. B* **56**, 9386 (1997).
- [5] R. Maezono, S. Ishihara, and N. Nagaosa, *Phys. Rev. B* **57**, R13993 (1998).
- [6] T. Nakajima, H. Kageyama, M. Ichihara, K. Ohoyama, H. Yoshizawa, and Y. Ueda, *J. Solid State Chem.* **177**, 987 (2004).
- [7] D. Akahoshi, M. Uchida, Y. Tomioka, T. Arima, Y. Matsui, and Y. Tokura, *Phys. Rev. Lett.* **90**, 177203 (2003).
- [8] D. Akahoshi, Y. Okimoto, M. Kubota, R. Kumai, T. Arima, Y. Tomioka, and Y. Tokura, *Phys. Rev. B* **70**, 064418 (2004).
- [9] T. Arima, D. Akahoshi, K. Oikawa, T. Kamiyama, M. Uchida, Y. Matsui, and Y. Tokura, *Phys. Rev. B* **66**, 140408(R) (2002).
- [10] C. Autret, A. Maignan, C. Martin, M. Hervieu, V. Hardy, S. Hébert, and B. Raveau, *Appl. Phys. Lett.* **82**, 4746 (2003).
- [11] F. Millange, V. Caignaert, B. Domenges, B. Raveau, and E. Suard, *Chem. Mater.* **10**, 1974 (1998).
- [12] H. Kageyama, T. Nakajima, M. Ichihara, Y. Ueda, H. Yoshizawa, and K. Ohoyama, *J. Phys. Soc. Jpn.* **72**, 241 (2003).
- [13] T. Nakajima and Y. Ueda, *J. Alloys Compd.* **383**, 135 (2004).
- [14] T. Nakajima, H. Kageyama, H. Yoshizawa, and Y. Ueda, *J. Phys. Soc. Jpn.* **71**, 2843 (2002).
- [15] A. J. Williams and J. P. Attfield, *Phys. Rev. B* **72**, 024436 (2005).
- [16] M. García-Fernández, U. Staub, Y. Bodenthin, S. M. Lawrence, A. M. Mulders, C. E. Buckley, S. Weyeneth, E. Pomjakushina, and K. Conder, *Phys. Rev. B* **77**, 060402(R) (2008).
- [17] D. Morikawa, K. Tsuda, Y. Maeda, S. Yamada, and T. Arima, *J. Phys. Soc. Jpn.* **81**, 093602 (2012).
- [18] E. A. Nowadnick, J. He, and C. J. Fennie, *Phys. Rev. B* **100**, 195129 (2019).
- [19] Q. Zhang, F. Guillou, A. Wahl, Y. Bréard, and V. Hardy, *Appl. Phys. Lett.* **96**, 242506 (2010).
- [20] T. Nakajima, H. Kageyama, H. Yoshizawa, K. Ohoyama, and Y. Ueda, *J. Phys. Soc. Jpn.* **72**, 3237 (2003).
- [21] S. Yamada, H. Sagayama, K. Higuchi, T. Sasaki, K. Sugimoto, and T. Arima, *Phys. Rev. B* **95**, 035101 (2017).
- [22] J. Blasco, G. Subías, M. L. Sanjuán, J. L. García-Muñoz, F. Fauth, and J. García, *Phys. Rev. B* **103**, 064105 (2021).
- [23] R. D. Mero, K. Ogawa, S. Yamada, and H.-L. Liu, *Sci. Rep.* **9**, 18164 (2019).
- [24] B. F. Buxton, J. A. Eades, J. W. Steeds, and G. M. Rackham, *Philos. Trans. R. Soc. A Math. Phys. Sci.* **281**, 171 (1976).
- [25] M. Tanaka, R. Saito, and H. Sekii, *Acta Crystallogr. Sec. A: Found. Crystallog.* **39**, 357 (1983).

- [26] M. Tanaka, H. Sekii, and T. Nagasawa, *Acta Crystallogr. Sec. A: Found. Crystallog.* **39**, 825 (1983).
- [27] M. Tanaka, *Acta Crystallogr. Sec. A: Found. Crystallog.* **50**, 261 (1994).
- [28] M. Tanaka, *International Tables for Crystallography*, 3rd ed., edited by U. Shmueli, Vol. B (IUCr, Springer, Dordrecht, 2008), pp. 307–356.
- [29] M. Tanaka and K. Tsuda, *J. Electron Microsc.* **60**(Supplement 1), S245 (2011).
- [30] Y. Ogata, K. Tsuda, and T. Hashimoto, *Jpn. J. Appl. Phys.* **47**, 4664 (2008).
- [31] Y. Shi, Y. Guo, X. Wang, A. J. Princep, D. Khalyavin, P. Manuel, Y. Michiue, A. Sato, K. Tsuda, S. Yu *et al.*, *Nat. Mater.* **12**, 1024 (2013).
- [32] K. Tsuda and M. Tanaka, *Acta Crystallogr. Sec. A: Found. Crystallog.* **51**, 7 (1995).
- [33] P. Hohenberg and W. Kohn, *Phys. Rev.* **136**, B864 (1964).
- [34] W. Kohn and L. J. Sham, *Phys. Rev.* **140**, A1133 (1965).
- [35] G. B. Bachelet, D. R. Hamann, and M. Schlüter, *Phys. Rev. B* **26**, 4199 (1982).
- [36] P. Giannozzi, S. Baroni, N. Bonini, M. Calandra, R. Car, C. Cavazzoni, D. Ceresoli, G. L. Chiarotti, M. Cococcioni, I. Dabo *et al.*, *J. Phys.: Condens. Matter* **21**, 395502 (2009).
- [37] F. Giustino, *Materials Modelling using Density Functional Theory: Properties and Predictions*, 1st ed. (Oxford University Press, Oxford, 2014), pp. 19–62.
- [38] H. J. Monkhorst and J. D. Pack, *Phys. Rev. B* **13**, 5188 (1976).
- [39] D. Vanderbilt, *Phys. Rev. B* **41**, 7892 (1990).
- [40] J. P. Perdew, K. Burke, and M. Ernzerhof, *Phys. Rev. Lett.* **77**, 3865 (1996).
- [41] K. Tsuda and M. Tanaka, *Acta Crystallogr. Sec. A: Found. Crystallog.* **55**, 939 (1999).
- [42] K. Tsuda, Y. Ogata, K. Takagi, T. Hashimoto, and M. Tanaka, *Acta Crystallogr. Sec. A: Found. Crystallog.* **58**, 514 (2002).
- [43] Y. Ogata, K. Tsuda, and M. Tanaka, *Acta Crystallogr. Sec. A: Found. Crystallog.* **64**, 587 (2008).
- [44] See Supplemental Material at <http://link.aps.org/supplemental/10.1103/PhysRevB.105.174114> for details about the zone-axis CBED patterns of [010] and [110] incidences at RT, tilted CBED patterns at RT and LT phases, 3D view of the optimized structures, estimated values of Debye-Waller factors, comparison of experimental and simulated CBED patterns, estimated thickness of the CBED patterns, and calculated BVSs of Mn atoms.
- [45] S. B. Wilkins, N. Stojić, T. A. W. Beale, N. Binggeli, C. W. M. Castleton, P. Bencok, D. Prabhakaran, A. T. Boothroyd, P. D. Hatton, and M. Altarelli, *Phys. Rev. B* **71**, 245102 (2005).
- [46] M. Uchida, D. Akahoshi, R. Kumai, Y. Tomioka, T. Arima, Y. Tokura, and Y. Matsui, *J. Phys. Soc. Jpn.* **71**, 2605 (2002).
- [47] D. Akahoshi, M. Uchida, T. Arima, Y. Tomioka, and Y. Tokura, *Phys. Rev. B* **74**, 012402 (2006).